

Predictive 3D modelling of free oblique cutting with an ANN-based material constitutive model and experimental validation over a wide range of conditions

F. Ducobu^{a,*}, O. Pantalé^b, B. Lauwers^c

^a*Machine Design and Production Engineering Lab, Research Institute for Science and Material Engineering, UMONS, Belgium*

^b*Laboratoire Génie de Production, INP/ENIT, Université de Toulouse, Tarbes, France*

^c*Department of Mechanical Engineering, KU Leuven & Flanders Make@KU Leuven-MaPS, Belgium*

Abstract

Modelling of the cutting process needs to move from 2D to 3D configurations to get closer to industrial applications. This study introduces a predictive 3D finite element model of free orthogonal and oblique cutting with an ANN-based material flow law and experimental validation in strictly the same conditions (cutting and geometrical). The flow law based on a neural network allows simulating the cutting process based on data coming from the material characterization tests without requiring any postulate concerning the expression of the flow law. The developments are applied to the formation of continuous chips for the titanium alloy Ti6Al4V and an unseen broad range of 36 cutting conditions is considered: 2 cutting edge inclinations, 3 uncut chip thicknesses and 6 cutting speeds. The predictive performance of the model (i.e., the evaluation of the trends of fundamental variables with the absence of tuning of both numerical parameters and model features when cutting conditions are significantly modified) is high for the forces, mainly cutting and passive, and the chip thickness ratio on all 36 cutting conditions. The accuracy of the main cutting force is excellent: the average difference with the experiments is 4 %, within the experimental dispersion. No significant degradation of the results is brought by the apparition of the third, out-of-plane, force, which shows the ability of the model to handle orthogonal and oblique cutting configurations.

*Corresponding author. Tel.: +32 65 45 68

Email address: Francois.Ducobu@umons.ac.be (F. Ducobu)

[FD:] Add a comment on ANN? [OP:] A new sentence has been introduced in the abstract

Keywords:

Oblique cutting, Finite element method (FEM), Predictive model, Artificial Neural Network (ANN)

1. Introduction

Selection of the tools and the cutting conditions in machining, but also comprehension of the influence of the process parameters on the quality of a component and its optimization, are still difficult to achieve because of the high level of complexity and the related nonlinear phenomena. In the frame of digital manufacturing and Industry 4.0, modelling the cutting process supports them, while remaining a challenging task. As highlighted by Arrazola et al. [1], most finite element (FE) models are developed in 2D (orthogonal cutting configuration usually) although industrial applications require 3D modelling.

Experimental validation of a model is a crucial step in modelling the cutting process. The experimental configuration should be as close as possible to the simulation. For the validation of orthogonal cutting, a rotational motion usually generates the cutting speed. This is often done in turning [2] or milling [3] and the diameter of the rotating workpiece must be large enough to reduce the influence of curvature on the results. Experimental configurations under strictly orthogonal cutting conditions are less often adopted, for example on broaching machines [4] or milling machines [5, 6]. If they remove the assumptions related to the rotary cutting motion, they generally allow lower cutting speeds (except on a dedicated machine, as in Afrasiabi et al. [7]). Free oblique cutting with a straight cutting edge has not yet been studied: all efforts have been concentrated on orthogonal cutting (mainly for 2D validation).

Lagrangian and Eulerian formulations are the most used for FE modelling of the cutting process. Combinations of formulations, such as Arbitrary Lagrangian-Eulerian (ALE) and Coupled Eulerian-Lagrangian (CEL), are increasingly being used to avoid (or reduce) mesh distortions [8]. The CEL formulation has recently been successfully applied to the modelling of cutting (2D orthogonal configuration): it provides accurate results with realistic chip shape and no mesh distortion. The first 3D applications are found in recent works [3, 9–12]. They cover orthogonal (free) cutting or a simple 3D operation, while free oblique cutting has yet to be studied.

The behaviour of the machined material is one of the key aspects of a FE model [1, 13]. Research is very intense in this area, leading to a growing number of constitutive material models ranging from empirical models to physical models, some including microstructure effects [13]. The empirical thermo-elasto-viscoplastic Johnson-Cook (JC) model [14] is still the most widely used to this day:

$$\sigma^y = (A + B \varepsilon^{p^n}) \left(1 + C \ln \frac{\dot{\varepsilon}^p}{\dot{\varepsilon}_0^p} \right) \left(1 - \left[\frac{T - T_{\text{room}}}{T_{\text{melt}} - T_{\text{room}}} \right]^m \right) \quad (1)$$

In this model, the flow stress, σ^y , is a function of the plastic strain, ε^p , the plastic strain rate, $\dot{\varepsilon}^p$, and the temperature, T . It is composed of 3 terms describing independently the plastic, viscous and thermal aspects. One of the points in favour of its adoption is the rather limited number of parameters to be identified, 5: A , B , C , m and n . Here, $\dot{\varepsilon}_0^p$ is the reference plastic strain rate, while T_{room} and T_{melt} are respectively the ambient (room) and melting temperature. More recent models developed on this basis, such as that of Calamaz et al. [15], increase this number of parameters (for the particular Calamaz model to 9). Other authors have also used Zerilli-Armstrong model to simulate cutting processes [16]. The best description (in theory) of the behaviour is obtained at the cost of a greater complexity of the identification process and a reduction of the link with the physical meaning of the model.

One of the problems of modelling material behaviour for cutting simulation is the identification of parameters, especially as the experimental equipment does not allow the high levels of strain, strain rate and temperature of machining to be achieved [13]. Inverse identification is an alternative, but the uniqueness of the solution is not always guaranteed [1, 13]. Early work by Özel and Altan [17] used the least squares method to identify the input parameters of a FE model in an inverse manner. Shrot and Bäker [18] then used the Levenberg-Marquardt algorithm for their identification of the material parameters. They showed that similar results (cutting forces and chip morphology) could be obtained by different sets of parameters and thus highlighted the non-uniqueness of the solution of the inverse problem. In addition to the flow stress parameters, Klocke et al. [19] also identified the damage parameters. In more recent work, such as Bosetti et al. [20] and Denkena et al. [21], the approach to the inverse identification problem is shifting from optimization to Artificial Intelligence (AI) based methods. The Downhill Simplex Algorithm (DSA) is adopted by Bergs et al. [22] and by Hardt et al. [23] for AISI 1045. Stampfer et al. [24] also chose DSA when treating AISI 4140 quenched at 3 different temperatures. In [25], Hardt et al. showed

that Particle Swarm Optimization (PSO) was more efficient in solving the inverse problem than DSA, even though the computational time is still significant. In order to reduce the computational time, an Efficient Global Optimization algorithm (EGO) was recently introduced by Kugalur Palanisamy et al. [26]. They identified simultaneously the parameters of the material constitutive model and the friction model for Ti6Al4V. Most of these works highlight the non-uniqueness of the identification and they all require the definition of the analytical expression of the constitutive model.

This paper fills the gap in the oblique cutting literature by investigating both orthogonal and free oblique 3D cutting configurations, both experimentally and numerically. An artificial neural network (ANN), introduced in Pantalé et al. [27], is implemented in a FE cutting model for the first time in place of the JC analytical law. A wide range of cutting speeds (6), uncut chip thicknesses (3) and cutting edge inclination angles (2) resulting in 36 different conditions are considered to demonstrate the predictive capability of the FE model for the fundamental variables. The main objectives of a predictive model are the accurate modelling of trends in results as conditions change and the good agreement of predicted values with experimental values (exact values are not sought due to experimental dispersions). This type of model is intended to support future choices and developments without the need for experimental data. No assumptions are made about the geometry of the workpiece in the model (i.e. its width is the same as in experiments), while keeping the calculation time relevant for industrial applications. The developments are applied to the formation of continuous chips of the titanium alloy Ti6Al4V.

2. Experimental setup

A 3-axis GF Mikron VCE 600 Pro milling machine is used to perform dry orthogonal and oblique cutting tests on Ti6Al4V (grade 5 annealed at 750 °C for 1 h followed by air cooling) with the same kinematics as a shaper. As shown in Figure 1, the tungsten carbide tool (modified LCGN160602-0600-FG, CP500 from SECO) is fixed on a dedicated holder (modified CFHN-06 from SECO) and the sample to be cut is clamped in the spindle (no rotation is allowed during the test). The top of the sample has 3 ribs of 1 mm width (the width of the tool is 6 mm) and 10 mm length. The test consists of removing the top layer (its height is the thickness of the uncut chip, h) of a rib at the prescribed cutting speed, v_c . The cutting speed is provided by the feed rate, v_f , of the machine (maximum value of 40 m/min). The inclination of the cutting edge of the tool, λ_s , results from the

96 relative angular orientation of the tool and the sample. Table 1 shows the cutting
 97 conditions: 6 cutting speeds, 3 uncut chip thicknesses and 2 inclination angles,
 98 each repeated 3 times.

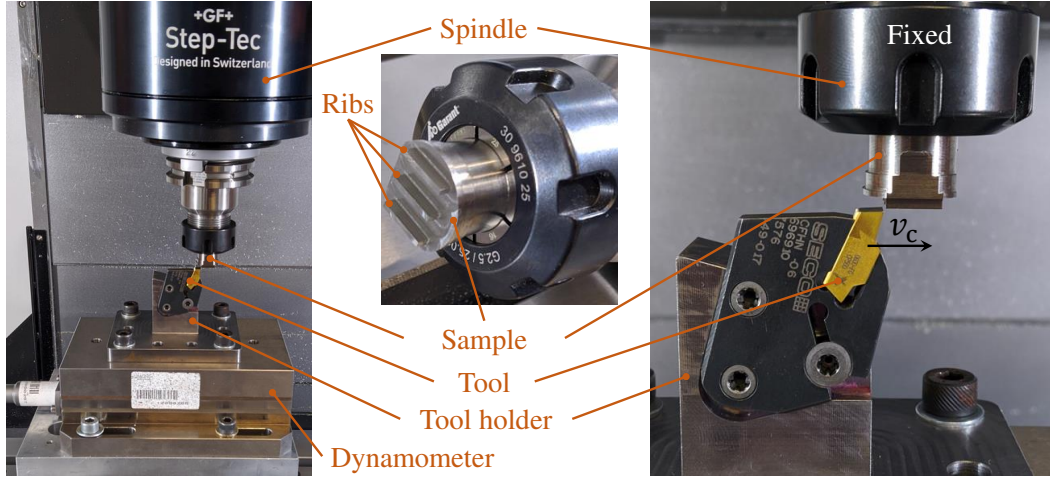


Figure 1: Experimental setup

Table 1: Cutting conditions of the study

Parameter	Values
Cutting speed, v_c (m/min)	5, 7.5, 10, 20, 30, 40
Uncut chip thickness, h (μm)	40, 60, 80
Cutting edge inclination, λ_s ($^\circ$)	0, 6
Width of the workpiece (mm)	1
Length of the workpiece (mm)	10
Width of the cutting edge (mm)	6 (1.1 in the model)
Cutting edge radius, r_β (μm)	20
Rake angle, γ_0 ($^\circ$)	15
Clearance angle, α_0 ($^\circ$)	2

99 Forces are measured with a 3-component Kistler 9257B dynamometer and
 100 are amplified by a Kistler 5070A charge amplifier. Acquisition is performed at
 101 3 kHz using a Kistler 5697A2 data acquisition system and DynoWare software.

102 The recorded forces are then filtered with a second-order low-pass Bessel filter at
 103 750 Hz before calculating the average value of the steady state signal.
 104 All chips are collected and observed with a Dino Lite digital microscope
 105 AM7013MZT (5 MP, magnification 20× – 250×). Each chip is measured 3 times
 106 along its length in order to obtain an average value representative of the whole
 107 chip.

108 3. Finite element model

109 3.1. Modelling choices

110 The CEL formulation is adopted to model the dry orthogonal and oblique cut-
 111 ting tests with Abaqus/Explicit 2020. The 3D model is composed of a fixed La-
 112 grangian tool and an Eulerian part (Figure 2). Chip formation occurs by plastic
 113 flow through the Eulerian domain without mesh distortion. The Eulerian formu-
 114 lation allows for chip formation without damage properties, by removing modelling
 115 assumptions. These two features contribute to the cutting models providing accu-
 116 rate results and realistic chips [8].

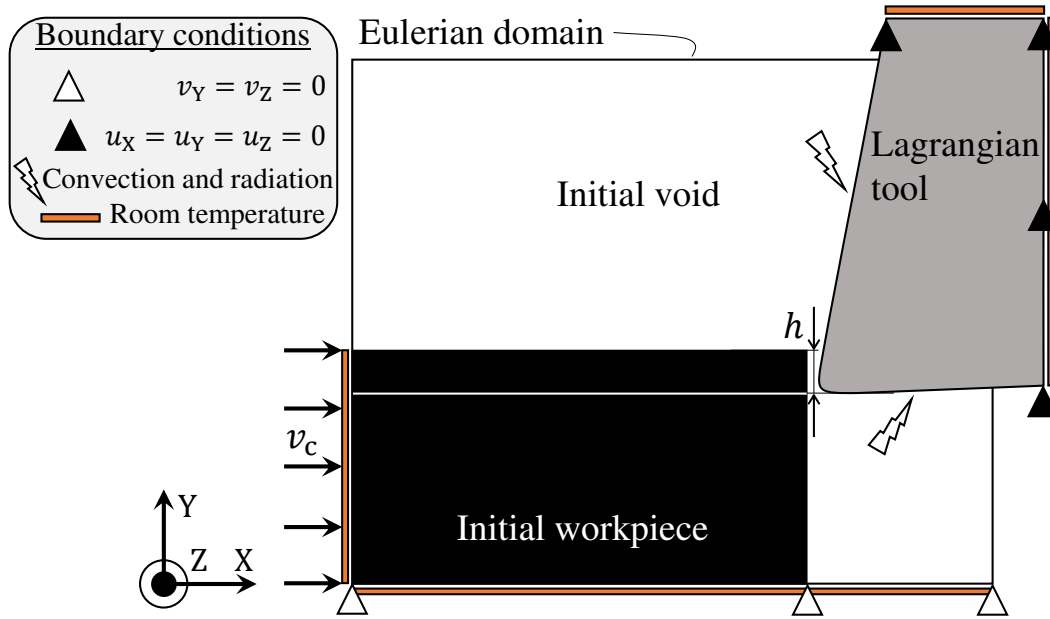


Figure 2: Boundary conditions and schematic initial geometry of the model

117 As shown in Figure 3, the full width of the workpiece (1 mm), i.e. one rib
 118 in the experiments, is modelled. To allow for chip formation and lateral flow,

119 the Eulerian domain is wider (it includes the volume in which the material can
 120 move). The volume above the initial part is also meshed with Eulerian elements
 121 for the same reasons. As in the experiments and to satisfy the assumption of
 122 an orthogonal and oblique free cut, the tool is wider than the workpiece (it is
 123 1.1 mm in the model and 6 mm in the experiments). It is very important to note
 124 that the models are the same for both inclination angles: they differ only in the
 125 rotation of the tool by 6° around the Y axis as in the experiments (Figure 3). This,
 126 together with the absence of assumptions when developing the models, contributes
 127 to make the models predictive: no input is changed when the cutting conditions
 128 are changed.

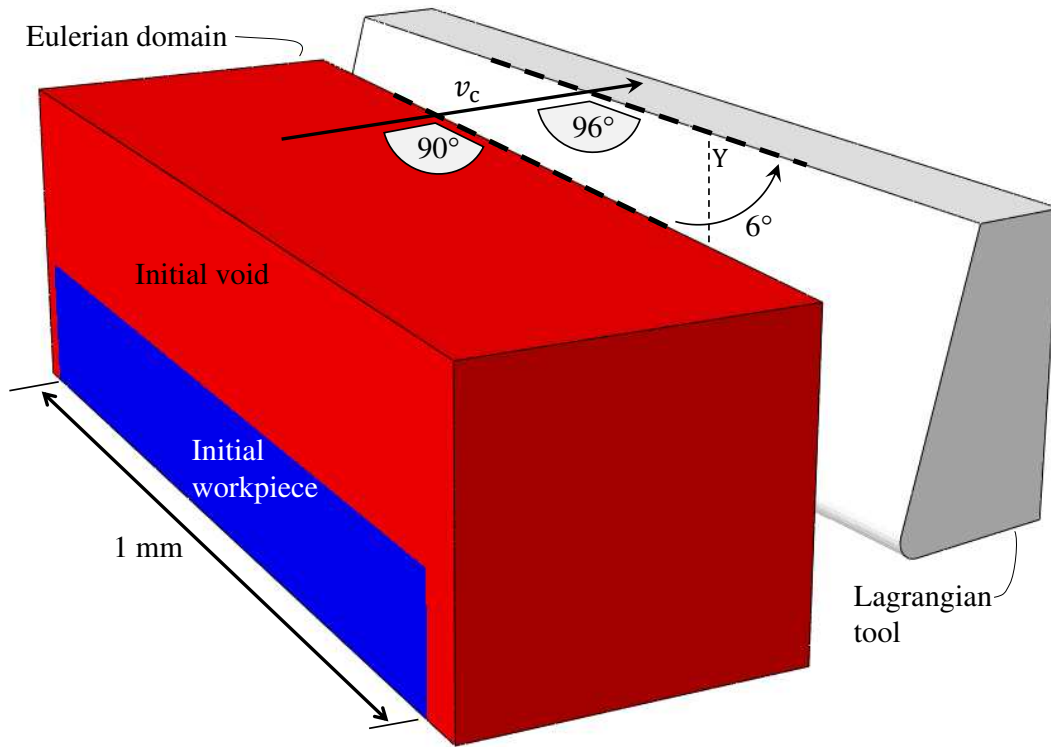


Figure 3: Configuration of the FE model for $\lambda_s = 6^\circ$

129 According to a previous sensitivity study of the mesh in orthogonal section
 130 with the CEL formulation [9], the edge size of the elements is $5 \mu\text{m}$ in the plane
 131 parallel to the cutting velocity. In the direction perpendicular to this plane, it is
 132 $5 \mu\text{m}$ in the areas close to the lateral limits of the Eulerian domain and $50 \mu\text{m}$ in
 133 the middle of the part. To reduce the computation time, the size of the model de-

134 depends on the value of the uncut chip thickness. This results in an Eulerian domain
 135 (EC3D8RT 8-node 3D linear Eulerian elements, coupled mechanical-thermal be-
 136 haviour and reduced integration) composed of 216 550 to 273 350 nodes and a La-
 137 grangian domain (C3D8T 8-node 3D linear Lagrangian elements, coupled mechanical-
 138 thermal behaviour) of 4650 nodes.

139 The Ti6Al4V part is assumed to be thermo-elasto-viscoplastic (isotropic) and
 140 the inelastic thermal fraction is 0.9. The JC parameter set of Seo et al. [28]
 141 is adopted because the value of A corresponds to the value of the typical yield
 142 strength of Ti6Al4V and this set was found to provide the best results among the
 143 20 sets available in the literature [29]. The TiN coated tungsten carbide tool is
 144 assumed to have linear elasticity. The material properties are given in Table 2.

Table 2: Materials properties [28, 30, 31]

Young's modulus, E (GPa)	Ti6Al4V	113.8 [†]
	WC	650
Poisson's ratio, ν	Ti6Al4V	0.34
	WC	0.2
Density, ρ (kg/m ³)	Ti6Al4V	4430
	WC	14 850
Conductivity, k (W/m K)	Ti6Al4V	6.3 [†]
	WC	100
Expansion, α (1/K)	Ti6Al4V	8.6E-6 [†]
	WC	5E-6
Specific heat, c_p (J/kg K)	Ti6Al4V	531 [†]
	WC	202
JC constitutive model	A (MPa)	997.9
	B (MPa)	653.1
	C	0.0198
	m	0.7
	n	0.45
	$\dot{\epsilon}_0$ (1/s)	1
	T_{room} (K)	293
	T_{melt} (K)	1873

[†]: Dependence on the temperature, value provided at 293 K

145 According to the experimental results of Rech et al. [32], it is assumed that
 146 Coulomb friction occurs at the tool-piece interface and that the coefficients of

147 friction, μ , and heat sharing, β , depend on the cutting speed. The limiting shear
 148 stress, τ_{\max} , is included and is given by:

$$\tau_{\max} = \frac{\text{yield stress}}{\sqrt{3}} = \frac{A}{\sqrt{3}} \quad (2)$$

149 All the friction energy is converted into heat. Table 3 shows the friction coef-
 150 ficients adopted in this study.

Table 3: Friction and heat transfer coefficients [30, 32]

Cutting speed, v_c (m/min)	μ	β
5	0.24	1
7.5	0.22	0.89
10	0.21	0.80
20	0.19	0.63
30	0.18	0.55
40	0.17	0.50
Limiting shear stress, τ_{\max} (MPa)	576	
Convection, U (W/m ² K)	50	
Radiation, ϵ	0.3	

151 An ambient temperature of 293 K is imposed on the top and right surfaces
 152 of the tool and on the left and bottom surfaces of the workpiece (Figure 2). It
 153 is assumed that radiation and convection occur on the rake and clearance faces
 154 of the tool. The initial temperature of the tool and workpiece is set to the room
 155 temperature (293 K). The heat transfer coefficients are provided in Table 3.

156 3.2. Material constitutive model of Ti6Al4V

157 [OP:] This section has been enhanced and completed

158 The constitutive model of the Ti6Al4V material used in all the numerical sim-
 159 ulations proposed in the section 4 is a thermo-elasto-viscoplastic law using a flow
 160 criterion based on an Artificial Neural Network (ANN) identified for the cho-
 161 sen material and implemented in the Abaqus/Explicit code via a Fortran subrou-
 162 tine VUHARD as proposed by Pantalé et al. in [27]. The principle of this ap-
 163 proach consists in replacing the analytical formulation of the flow law, based on
 164 a Johnson-Cook or Zerilli-Armstrong type model, and allowing the calculation of

the flow stress σ^y as a function of the plastic strain ε^p , the plastic strain rate, $\dot{\varepsilon}^p$, and the temperature T , by a multi-layer ANN serving as universal approximator. Thus, the parameters of the neural network can be directly identified from the experimental data without having to postulate a behavioural model, which simplifies the procedure and allows greater flexibility in the definition of the model. The proposed approach also allows, as shown in Pantalé et al. [27], to compute the three derivatives of the flow stress σ^y with respect to the three input variables of the model, a necessary step to implement this model as a flow law in the form of a VUHARD subroutine in the FEM code Abaqus/Explicit, using the exact same network architecture and identified trained parameters as the one used to compute the flow stress σ^y .

In order to verify the influence of the neural network complexity on the numerical results of the simulation and on the computation time, several ANN architectures are tested afterwards (in 3.4). The chosen global architecture has 2 hidden layers with a variable number of neurons for the first hidden layer ($\zeta = 9$ to 17) and 7 neurons for the second hidden layer, 3 inputs (the plastic strain, ε^p , the plastic strain rate, $\dot{\varepsilon}^p$, and the temperature, T) and one output (the yield strength, σ^y). The global architecture of this type of ANN is given in Figure 4 for 9 neurons in the first hidden layer. According to Pantalé et al. [27], this ANN is referred to as ANN 3-9-7-1-sig, as it has 3 inputs, 9 neurons in the first hidden layer, 7 neurons in the second hidden layer, 1 output and a sigmoid activation function.

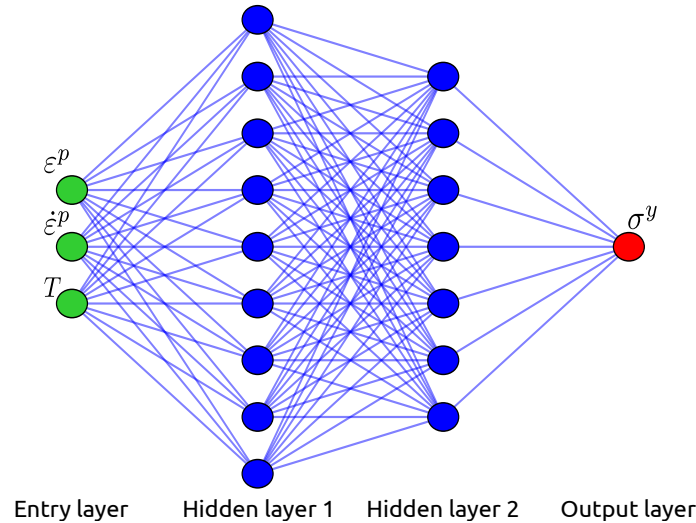


Figure 4: Architecture of the ANN 3-9-7-1-sig used for the flow law

186 In a preliminary phase, after having selected the global architecture of the neu-
 187 ral network, it is necessary to proceed to its training from some inputs. The inputs
 188 for this application were generated from the Johnson-Cook flow law expression
 189 reported in Equation (1) and the identified parameters reported in Table 2. This
 190 approach was chosen to demonstrate the ability of the neural network flow law to
 191 replace a classically formulated flow law such as Johnson-Cook's for the simu-
 192 lation of metal cutting. In future developments, experimental tests on a Gleeble
 193 thermomechanical simulator will be used to generate this network training data.
 194 The training data, presented in the form of a data table containing the plastic strain
 195 ε^p , the plastic strain rate $\dot{\varepsilon}^p$, the temperature T and the flow stress σ^y , is processed
 196 by a learning algorithm, developed at LGP, in Python, using the Tensorflow li-
 197 brary. One hour of training on a Dell XPS13 7390 laptop running Ubuntu 20.04
 198 64 bits with 16 GiB of Ram and an Intel 4-core i7-10510U processor allow ob-
 199 taining the converged parameters of the ANN model.

200 Once this learning phase is completed, the neural network parameters result-
 201 ing from the learning process are used directly by a Python program, in charge
 202 of automatically generating the Fortran source code of the VUHARD subroutine
 203 in order to compute the flow stress σ^y and its three derivatives, required for the
 204 explicit Abaqus FEM code.

205 The main advantage of this approach (the use of an ANN), after the learning
 206 phase, is that, for example, the output σ^y of the network is now linked to the inputs
 207 ε^p , $\dot{\varepsilon}^p$, and T by the equations (3) to (7) for a two hidden layers neural network
 208 with a sigmoid activation function as proposed previously.

209 Thus, in the VUHARD subroutine, the computation of the flow stress σ^y from
 210 the 3 input variables ε^p , $\dot{\varepsilon}^p$, and T is performed using the following procedure.
 211 The first step is to scale the input data to the interval $[0, 1]$ using the following
 212 equation:

$$\vec{x} = \begin{cases} x_1 = \frac{\varepsilon^p - [\varepsilon^p]_{min}}{[\varepsilon^p]_{max} - [\varepsilon^p]_{min}} \\ x_2 = \frac{\ln(\dot{\varepsilon}^p) - [\ln(\dot{\varepsilon}^p)]_{min}}{[\ln(\dot{\varepsilon}^p)]_{max} - [\ln(\dot{\varepsilon}^p)]_{min}} \\ x_3 = \frac{T - [T]_{min}}{[T]_{max} - [T]_{min}} \end{cases} \quad (3)$$

where quantities $[]_{min}$ and $[]_{max}$ are the boundaries of the range of the corre-
 sponding field during the training phase. Corresponding values, for the proposed
 case, are given in Appendix A. According to the architecture of the network,
 the outputs of the neurons of the first hidden layer \vec{y}_1 are given by the following

equation:

$$\vec{y}_1 = \text{sig}\left(\mathbf{w}_1 \cdot \vec{x} + \vec{b}_1\right) \quad (4)$$

where, \mathbf{w}_1 and \vec{b}_1 are the weights and biases associated with the first hidden layer and $\text{sig}()$ is the sigmoid activation function defined by the equation (5) :

$$\text{sig}(x) = \frac{1}{1 + e^{-x}} \quad (5)$$

Then, the output of the neurons of the second hidden layer is given by the equation (6) :

$$\vec{y}_2 = \text{sig}\left(\mathbf{w}_2 \cdot \vec{y}_1 + \vec{b}_2\right) \quad (6)$$

where, \mathbf{w}_2 and \vec{b}_2 are the weights and biases associated with the second hidden layer. Finally, the σ^y output of the ANN is thus given by the equation (7) :

$$\sigma^y = ([\sigma^y]_{\max} - [\sigma^y]_{\min}) \left(\vec{w}^T \cdot \vec{y}_2 + b \right) + [\sigma^y]_{\min} \quad (7)$$

213 where, \vec{w} and b are the weights and the bias associated with the output layer.

On the other hand, the three derivatives of the yield stress σ^y with respect to the three input variables ε^p , $\dot{\varepsilon}^p$, and T are given by the equation (8):

$$\begin{cases} \partial\sigma^y/\partial\varepsilon^p = s'_1 \frac{[\sigma^y]_{\max} - [\sigma^y]_{\min}}{[\varepsilon^p]_{\max} - [\varepsilon^p]_{\min}} \\ \partial\sigma^y/\partial\dot{\varepsilon}^p = s'_2 \frac{[\sigma^y]_{\max} - [\sigma^y]_{\min}}{[\dot{\varepsilon}^p]_{\max} - [\dot{\varepsilon}^p]_{\min}} \dot{\varepsilon}^p \\ \partial\sigma^y/\partial T = s'_3 \frac{[\sigma^y]_{\max} - [\sigma^y]_{\min}}{[T]_{\max} - [T]_{\min}} \end{cases} \quad (8)$$

where s'_i is the i^{th} component of the vector \vec{s}' defined by the equation (9):

$$\vec{s}' = \mathbf{w}_1^T \cdot \left[\mathbf{w}_2^T \cdot \left(\frac{\vec{w} \circ e^{-\vec{y}_2}}{[1 + e^{-\vec{y}_2}]^2} \right) \circ \left(\frac{e^{-\vec{y}_1}}{[1 + e^{-\vec{y}_1}]^2} \right) \right] \quad (9)$$

214 and \circ is the elements-wise product, known as the Hadamard product. In equa-
 215 tions (3) to (9), quantities \mathbf{w}_1 , \mathbf{w}_2 , \vec{w} , \vec{b}_1 , \vec{b}_2 and b are evaluated by the training
 216 procedure of the ANN. Corresponding values for an ANN containing 9 neurons
 217 in the first hidden layer and 7 neurons in the second hidden layer are reported in
 218 Appendix A. The set of equations (3) to (9), together with the network paramete-
 219 rs identified in the learning phase, is automatically translated into a VUHARD
 220 Fortran subroutine used by the FEM code Abaqus to simulate the cutting model.

Because of the large number of identified parameters for all the ANN models (from 114 to 202 for 9 and 17 neurons for the first hidden layer, respectively), the other 4 sets of ANN parameters used in this publication can be found in [33].

[FD:] Inclure dans corps du texte puisque article normal et rq reviewer?

[OP:] I think it should still be enough as we put a complete set in the appendix, no need to put everything concerning all networks (see final remark in Appendix)

3.3. Sensitivity study of the results to mass scaling

FE modelling of the cutting process is very expensive in terms of CPU time due to the coupling of many nonlinear phenomena and the large amount of tiny finite elements. Mass scaling (MS) is introduced into the model to reduce the CPU computation time while checking that it does not influence the results (forces and energies) via a mass scaling sensitivity study. MS factors, MS_f , ranging from 1E6 (theoretical CPU time scale of $\sqrt{MS_f} = 1000$) to 1 (no scale) were used for a cut condition ($\lambda_s = 0^\circ$, $v_c = 30$ m/min and $h = 60$ μ m). The same signal processing procedure is applied to the numerical forces as to the experimental forces (cf. 2): they are filtered with a second order low-pass Bessel filter at 750 Hz before calculating the steady state average value. Table 4 gives the results of the model with MS normalized (\hat{F}_i) by those of the model without MS:

$$\hat{F}_i = \frac{F_i \text{ with MS}}{F_i \text{ without MS}} \quad (10)$$

with $i = c$ for the cutting force and $i = f$ for the feed force. As expected, the real speed does not increase linearly with the MS_f , but it remains significant. A MS_f of 1E6 leads to an unstable computation and a MS_f of 1E5 leads to erratic force evolutions. These results are confirmed by high values of the ratio of the kinetic (KE) to the internal (IE) energies (it should not exceed a few % [34, 35]). A value of MS_f of 1E3 is chosen as it offers a good balance between reducing the computation time and the impact on the forces, while keeping the $\frac{KE}{IE}$ below 1 %. To provide an order of magnitude of CPU computation time, between 10 h and 50 h (depending on the value of h) are required on 4 cores of an Intel i7-5700HQ CPU at 2.7–3.5 GHz.

3.4. Sensitivity study of the results to the number of neurons

The number of neurons in the hidden layers may influence the results. A sensitivity study on the number of neurons of the first hidden layer, ζ , is performed in order to select the ANN offering the best balance between CPU computation time and quality of the results. The results of the study are provided in Table 5.

Table 4: MS sensitivity study (selected MS factor, MS_f , in bold, \hat{F}_c : normalized cutting force, \hat{F}_f : normalized feed force, KE : kinetic energy, IE : internal energy)

MS_f	CPU scaling	Speed-up	\hat{F}_c	\hat{F}_f	$\frac{KE}{IE}$ (%)
1	1	1	1	1	2.3E-4
1E2	10	9	1.006	0.982	2.2E-2
1E3	32	21	1.008	0.940	2.2E-1
1E4	100	61	1.012	0.921	2.4
1E5	316	173	Erratic	Erratic	22
1E6	1000	207	Unstable	Unstable	58

254 The \check{F}_i corresponds to the results of the model with ANN normalized by those of
 255 the model with the built-in JC model:

$$\check{F}_i = \frac{F_i \text{ with ANN}}{F_i \text{ with JC}} \quad (11)$$

256 They show no influence on the numerical results for the forces compared to the
 257 built-in Johnson-Cook model, only the computation time is influenced by the num-
 258 ber of neurons in the first hidden layer and increases with it. This increase in com-
 259 putation time is not only due to the increasing complexity of the neural network
 260 with the number of neurons, but also to the need to go through a VUHARD user
 261 subroutine. A first hidden layer of 9 neurons is therefore selected as it leads to the
 262 smallest increase in CPU computation time, without influence on the final result.

Table 5: Sensitivity of the forces to the number of neurons of the first layer, ζ (selection in bold, \check{F}_c : normalized cutting force, \check{F}_f : normalized feed force)

ζ	Time increase (%)	\check{F}_c	\check{F}_f
Built-in	0	1.000	1.000
9	6	1.000	0.999
11	6	1.001	1.000
13	7	1.000	0.998
15	8	1.001	1.001
17	10	1.000	1.000

263 4. Experimental and numerical results

264 An example of the time evolution of the numerical and experimental forces
 265 is plotted for the 3 directions in Figure 5 at $\lambda_s = 6^\circ$, $v_c = 10$ m/min and $h =$
 266 40 m/min. The FE models are calculated up to a few microseconds after the sta-
 267 tionary state is reached. Then, a linear extrapolation (dashed line between the last
 268 two markers in Figure 5) is used to provide numerical values for the same time
 269 range as the experimental values. The average and standard deviation (2σ) are
 270 calculated from the 3 experimental values. The resulting dispersion is shown in
 271 Figure 5 around the average values of each force. Steady state takes longer to be
 272 reached for the experiments than for the numerical model, in particular for the
 273 cutting force. The dispersion around the evolution of the average force is greater
 274 for the feed force than for the cutting force, while the average value of the feed
 275 force is 46 % of the average value of the cutting force. The numerical cutting force
 276 is very close to the experimental average cutting force; it is only 4 % higher. This
 277 difference, Δj , is calculated by :

$$\Delta j = \frac{|j^{(\text{sim})} - j^{(\text{exp})}|}{j^{(\text{exp})}} \times 100 \quad (12)$$

278 where j is the cutting force, the feed force, the passive force or the chip thick-
 279 ness. $j^{(\text{sim})}$ is the average value from the simulation, while $j^{(\text{exp})}$ is the average
 280 experimental value.

281 The numerical feed force is underestimated by the model, but is within the
 282 95 % experimental confidence interval. The numerical passive force difference is
 283 also underestimated and is not within the narrowest experimental dispersion. The
 284 difference between the average values of the experimental and numerical feed and
 285 passive forces is 25 %. A less well modelled feed force than the cutting force is
 286 typical of FE models of the cutting process and the difference with the experi-
 287 mental value is similar to other studies for a narrower range of cutting conditions
 288 [7, 36–39]. Hardt and Bergs [12] also obtained larger differences for feed and
 289 passive force than for cutting force. The difference for passive force was higher
 290 than for feed force, which is the opposite observation of this work.

291 Numerical chips at $v_c = 10$ m/min and $h = 40$ μm for $\lambda_s = 0^\circ$ and $\lambda_s = 6^\circ$ are
 292 provided in Figures 6 and 7. When the inclination of the cutting edge is 0° , both
 293 sides of the chip are identical and a symmetry plane can be drawn in the middle
 294 of the workpiece (Figure 7 (a)). On the other hand, for a slope of the cutting edge
 295 of 6° , the chip is no longer aligned with the workpiece. The chip bends to one
 296 side due to the orientation of the tool and symmetry is lost in both the geometry

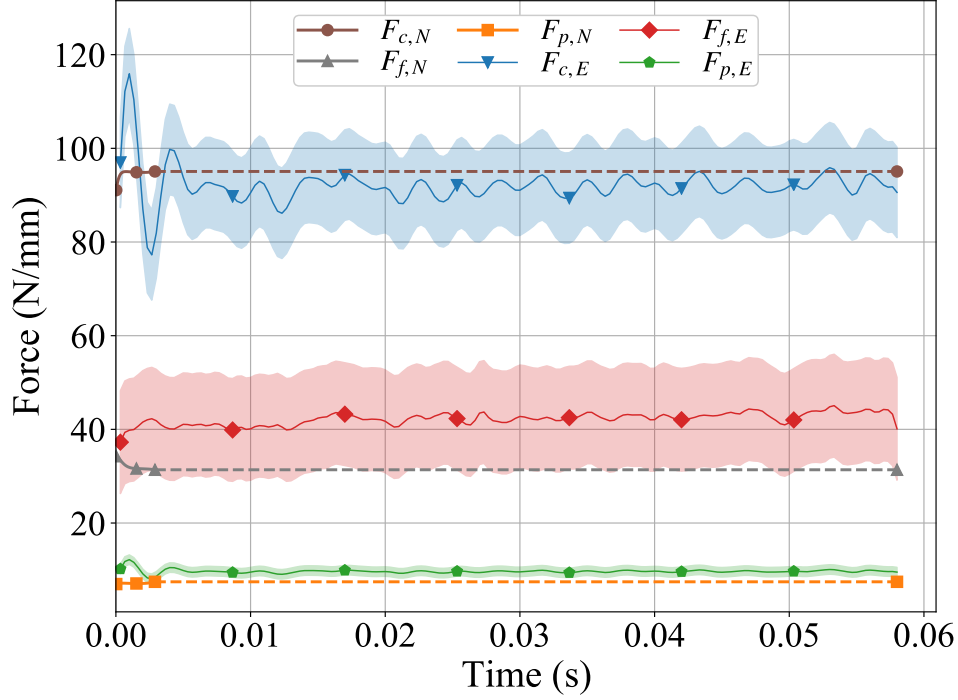


Figure 5: Temporal evolutions of experimental (E) and numerical (N) forces at $\lambda_s = 6^\circ$, $v_c = 10$ m/min and $h = 40$ μ m with dispersion around average experimental values (linear extrapolation of numerical values in dashed)

297 and the thermal and mechanical fields, as shown in figure 7 (b). This produces
 298 helical chips for the inclination angle of 6° as in the experiments. Figure 8 shows
 299 the variation of the chip thickness across its width: it is thicker in the middle
 300 (i.e. the body of the chip) than on its sides. This underlines the importance of
 301 3D modelling, even for the orthogonal cutting configuration as highlighted earlier
 302 [9]. The 3D modelling also allows reproducing the lateral flow that occurs in the
 303 experiments for both values of cutting edge inclination (Figure 6), unlike a 2D
 304 model [3, 9, 10]. Although this leads to higher computation times, future cutting
 305 models should be in 3D, even when orthogonal cutting is considered. In this
 306 case, it is recommended to take advantage of the symmetry of the configuration
 307 to reduce the computation time. This simplification has not been included in this
 308 study to avoid any difference in the FE models between the 2 inclinations of the

309 cutting edge.

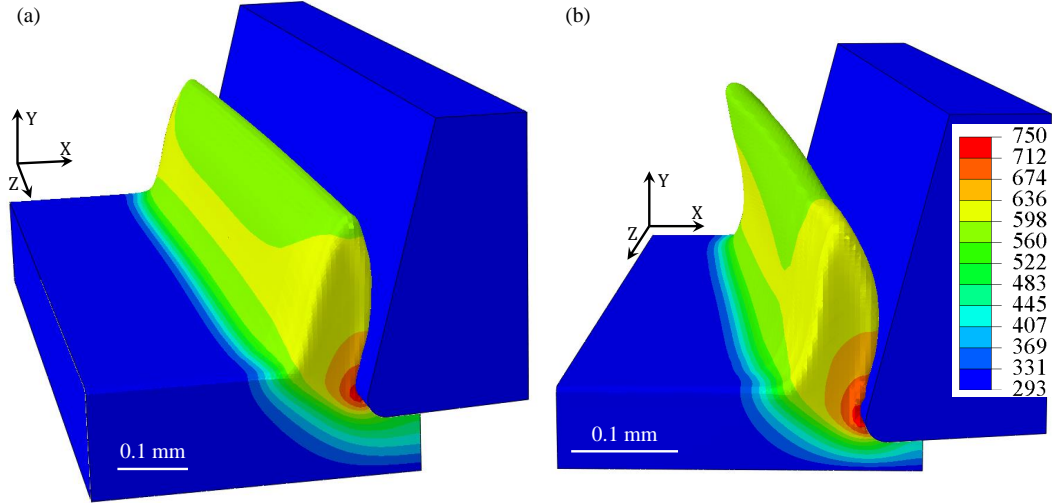


Figure 6: Temperature contours (in K) of the numerical chip after 1.5 ms at $v_c = 10$ m/min, $h = 40$ μ m and (a) $\lambda_s = 0^\circ$, (b) $\lambda_s = 6^\circ$

310 Average values of the experimental forces and their dispersion are shown in
 311 Figures 9 to 13 together with the average numerical values. Passive force values
 312 are of course only plotted for $\lambda_s = 6^\circ$ as they are equal to zero when $\lambda_s = 0^\circ$.

313 The increase in cutting force with uncut chip thickness is clearly observed in
 314 Figures 9 and 10 for both experimental and numerical results at the 2 inclination
 315 angles, as well as the decrease in force with increasing cutting speed. This shows
 316 that temperature softening dominates strain rate hardening for Ti6Al4V and is
 317 accurately modelled. Increasing the inclination angle from 0° to 6° slightly re-
 318 duces the cutting force; this is well captured by the model. For cutting speeds of
 319 20–40 m/min and an inclination angle of 0° , F_c is almost constant with cutting
 320 speed for uncut chip thicknesses of 40 μ m and 60 μ m, while it decreases slightly
 321 for 80 μ m; this small stabilization is less marked for the model.

322 An increase in the deviation around the average value with the cutting speed
 323 is noted for values above 10 m/min. All numerical values are within 95 % con-
 324 fidence of the experiments (35 of the 36 conditions are within 68 % confidence).
 325 The average difference with the experiments is 4 %, which is remarkable, also
 326 considering the wide range of cutting conditions considered and the absence of
 327 model tuning. This underlines the predictive ability and accuracy of the FE model
 328 for both inclination angles.

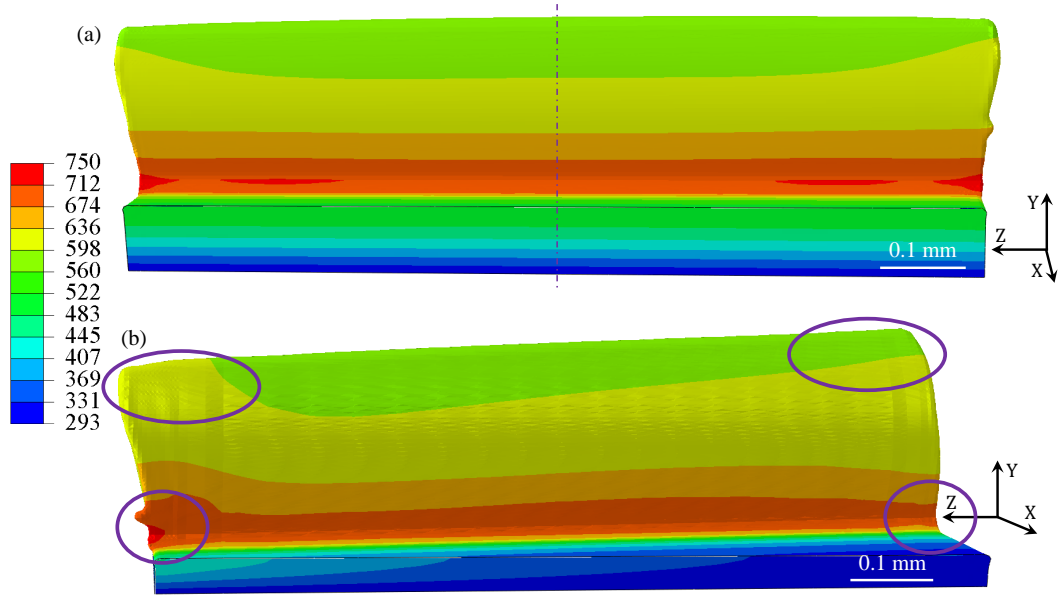


Figure 7: Temperature contours (in K) of the back of the numerical chip (tool is removed) after 1.5 ms at $v_c = 10$ m/min, $h = 40$ μ m and (a) $\lambda_s = 0^\circ$, (b) $\lambda_s = 6^\circ$

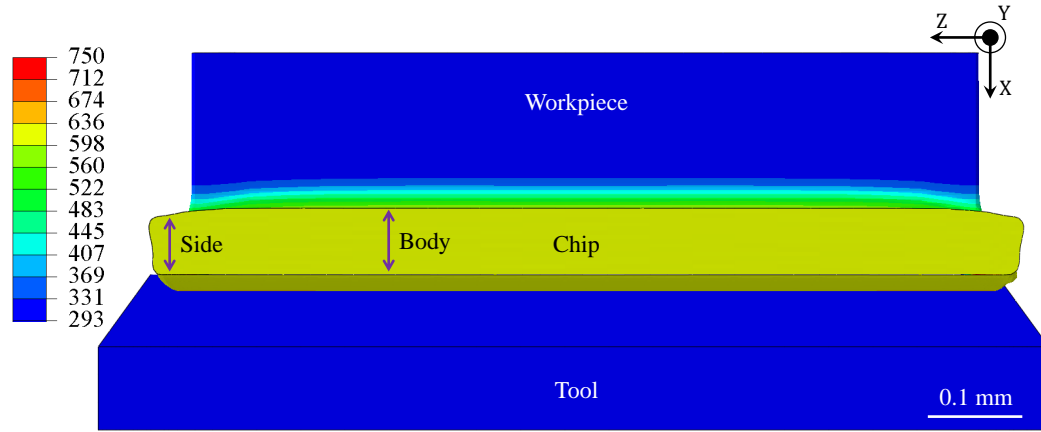


Figure 8: Temperature contours (in K) of the top of the numerical chip after 1.5 ms at $v_c = 10$ m/min, $h = 40$ μ m and $\lambda_s = 0^\circ$

329 Figures 11 and 12 show the results for the feed force, where the two clear-
 330 est trends for the experiments are its decrease with the inclination angle and its
 331 increase with the thickness of the uncut chip (even though it is lower than ex-

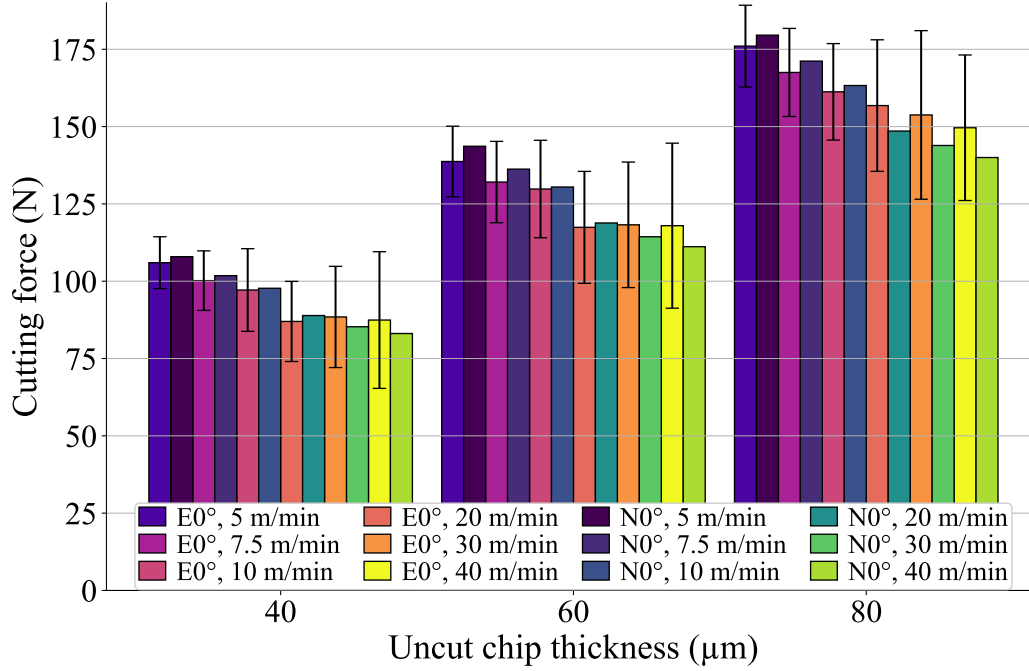


Figure 9: Comparison of experimental (E) and numerical (N) cutting forces at the cutting edge inclination of 0° for the 3 uncut chip thicknesses (40, 60 and 40 μm) and the 6 cutting speeds (5, 7.5, 10, 20, 30 and 40 m/min)

332 pected). For 80 μm , F_f decreases overall with v_c in the experiments. For 40 μm
 333 and 60 μm , the force decreases at lower v_c , then increases for 0° , while a decrease
 334 is observed at all v_c for 6° (the experimental dispersion is high for both inclination
 335 angles, but the average trend with cutting speed is clear at 6° , not at 0°). For the
 336 numerical values, the overall trend is the same for the 3 uncut chip thicknesses
 337 and the two inclination angles: a decrease for the lowest values of v_c and then an
 338 increase. It should be noted that the numerical model does not correctly handle the
 339 trends of the feed forces: as Figure 12 clearly shows, the numerical forces have an
 340 overall increasing trend with the cutting speed, while their average value mainly
 341 decreases when the uncut chip thickness increases. The differences between the
 342 average numerical and experimental values increase with the thickness of the un-
 343 cut chip: the forces are closer at 40 μm than at 80 μm . The numerical values are
 344 generally not within the 95 % confidence interval (they do not clearly change with
 345 the cutting conditions). Coupled with the differences in trends, this shows that
 346 F_f is less well modelled (the average difference is 39 %) than F_c as usual in FE

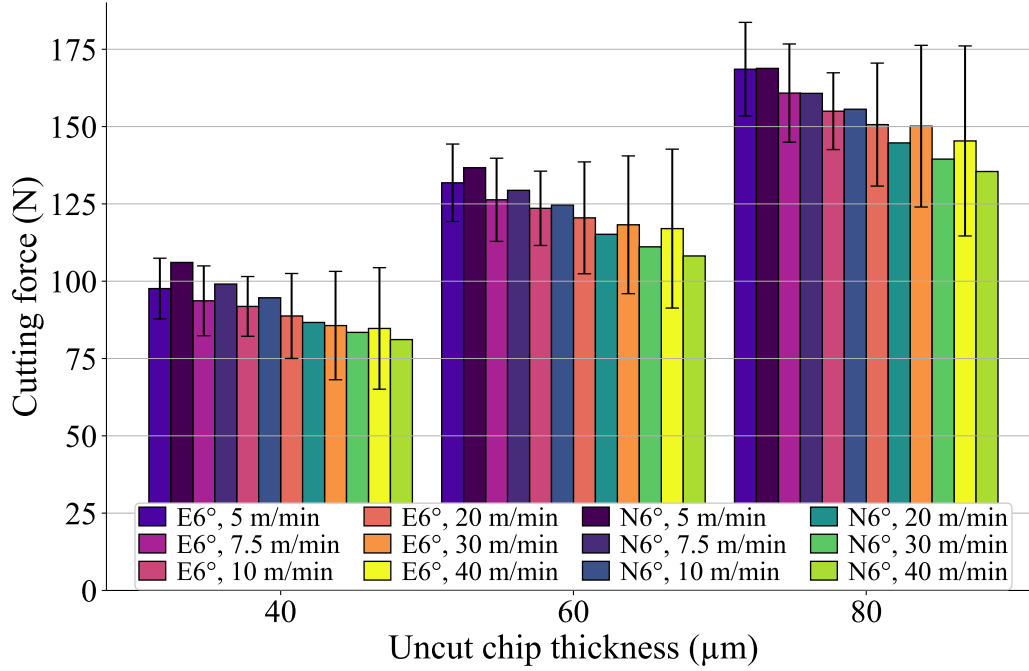


Figure 10: Comparison of experimental (E) and numerical (N) cutting forces at the cutting edge inclination of 6° for the 3 uncut chip thicknesses (40, 60 and $80 \mu\text{m}$) and the 6 cutting speeds (5, 7.5, 10, 20, 30 and 40 m/min)

modelling of the cutting process and even more so in 3D [12]. The influence of the uncut chip thickness on the feed force should therefore be improved. The parameters of the material constitutive model are known to have an impact on the forces (and on the chip morphology) [26, 29]. The friction model should also be improved to strengthen the results [12].

The passive force is non-zero for the inclination angle of 6° (Figure 13). Like the cutting force, it increases with the thickness of the uncut chip and decreases with the cutting speed. The comparison with experiments is broadly the same as for F_c , except for a greater difference in the magnitude of F_p (the average difference is 26 %, but it is small in absolute terms - less than 5 N). Most of the numerical values do not fall within the experimental 95 % confidence interval. A lower magnitude of the passive force from the simulation than from the experiments with the correct trends when the cutting conditions change was also observed by Hardt and Bergs [12]. The differences were mainly attributed to differences in cutting edge radius, friction modelling and material constitutive model. In this

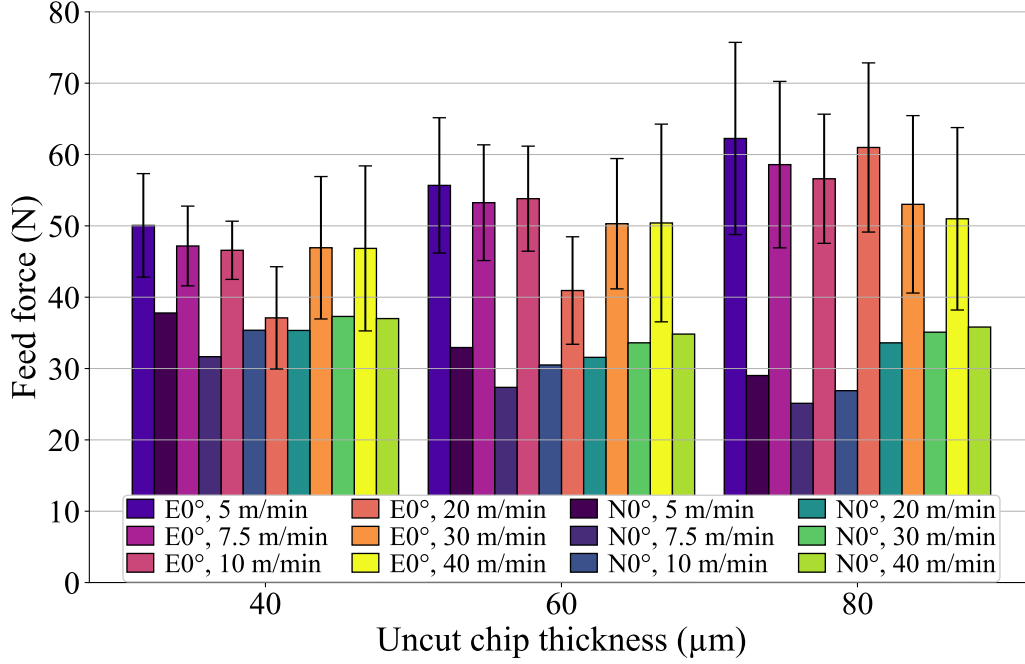


Figure 11: Comparison of experimental (E) and numerical (N) feed forces at the cutting edge inclination of 0° for the 3 uncut chip thicknesses (40, 60 and $80 \mu\text{m}$) and the 6 cutting speeds (5, 7.5, 10, 20, 30 and 40 m/min)

work, the impact of the cutting edge radius can be neglected as it is the same in the model as in the experiments.

As far as the chip morphology is concerned, all chips are continuous. For both the simulation and the experiments, the chip thickness ratio, λ_h :

$$\lambda_h = \frac{h'}{h} \quad (13)$$

with h the thickness of the uncut chip and h' the thickness of the chip, is almost independent of the thickness of the uncut chip (Figures 14 and 15). It is slightly reduced from $\lambda_s = 0^\circ$ to $\lambda_s = 6^\circ$, which means that the chip thickness decreases with the angle of inclination. This influence is underestimated by the model: the reduction of λ_h is smaller than in the experiments. The average difference between the experimental and numerical λ_h is 17 % over the whole range of cutting conditions. The chip thickness ratio decreases with cutting speed due to the reduction in friction, which is correctly accounted for by the model. As with the feed force, the

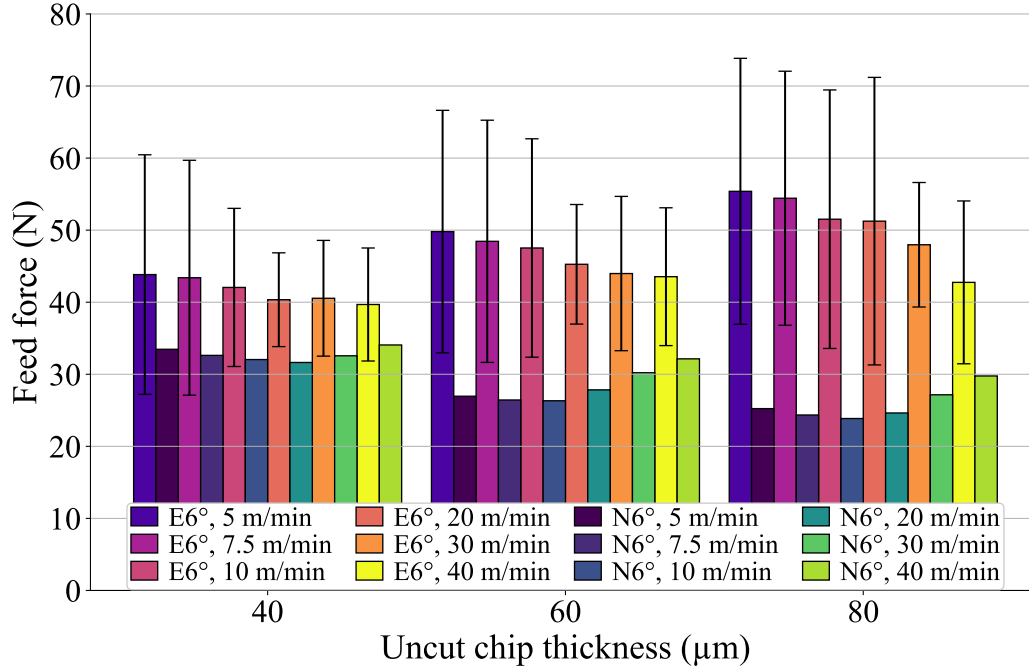


Figure 12: Comparison of experimental (E) and numerical (N) feed forces at the cutting edge inclination of 6° for the 3 uncut chip thicknesses (40, 60 and $80\ \mu\text{m}$) and the 6 cutting speeds (5, 7.5, 10, 20, 30 and $40\ \text{m/min}$)

372 results should be improved by more complex friction models and a set of material
 373 parameters for which the identification includes forces and chip thickness: [26].

374 The differences calculated according to the equation 12 are presented in Ta-
 375 ble 6 to provide a quantitative overview of the results. The cutting force is the
 376 best modelled quantity as observed in the literature. This result was to be ex-
 377 pected as the parameter set of the constitutive model was selected mainly due to
 378 its good approximation of the cutting force [29]. As this selection was made with
 379 a 2D model, the results show the ability of the model to correctly handle the third
 380 (passive) force. Based on the average differences, the performance of the model
 381 is very close for the cutting and feed forces for both inclinations of the cutting
 382 edge, although a small degradation (1 % and 2 %, respectively) is noted for 6° .
 383 This degradation is more important (7 %) for the chip thickness ratio and must
 384 be linked to the difference in passive force. Indeed, the chip thickness and out-of-
 385 plane force models are deeply linked. Improving the friction at the tool-workpiece
 386 interface should be a key point. It should be noted that the chip thickness is very

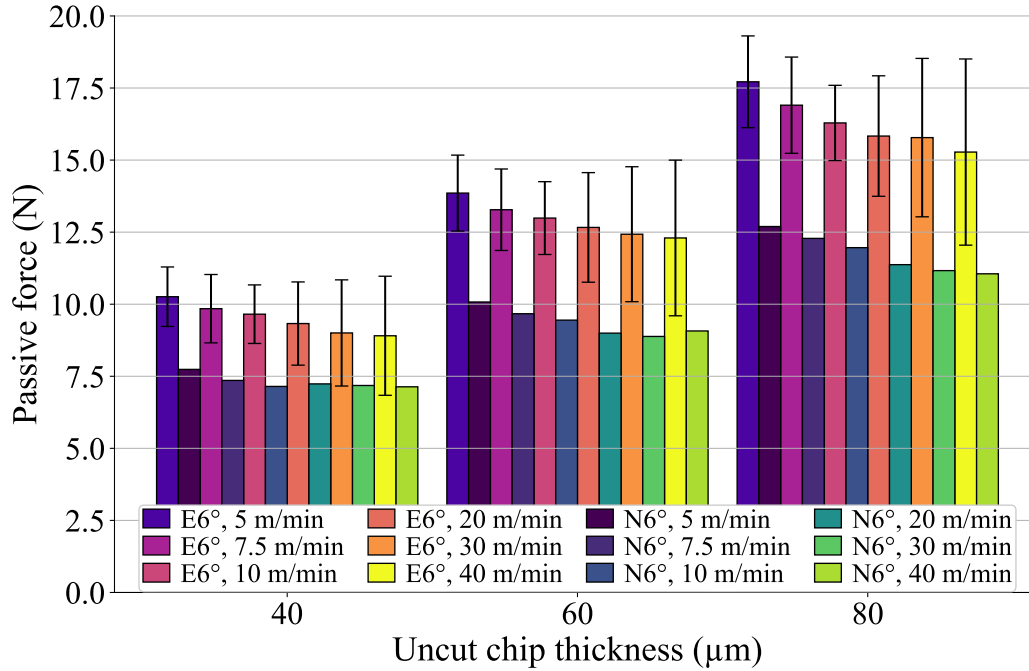


Figure 13: Comparison of experimental (E) and numerical (N) passive forces at the cutting edge inclination of 6° for the 3 uncut chip thicknesses (40, 60 and 80 μm) and the 6 cutting speeds (5, 7.5, 10, 20, 30 and 40 m/min)

well modelled under certain cutting conditions with a minimum difference of 2 %. The difference is larger for the feed force than for the passive force, a trend opposite to that of Hardt and Bergs. The average and range (min – max) of the differences are larger for the forward force. The smaller range of the passive force confirms a shift for all cutting conditions, similar to the results of Hardt and Bergs [12]. Again, the friction modelling should be the first aspect of the model to be improved in future developments.

5. Conclusions

An experimental and numerical study of the orthogonal and oblique free cutting of Ti6Al4V was carried out for a wide range of cutting conditions using an ANN-based material constitutive model. The following main conclusions are drawn:

- The experimental study was carried out with the same set-up in free orthog-

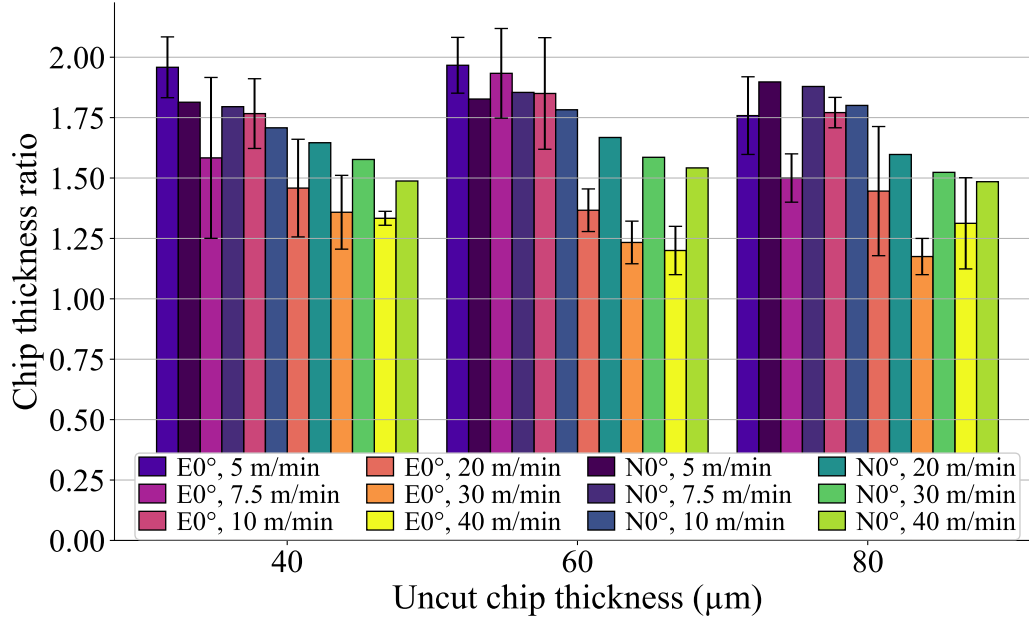


Figure 14: Comparison of experimental (E) and numerical (N) chip thickness ratios at the cutting edge inclination of 0° for the 3 uncut chip thicknesses (40, 60 and $80 \mu\text{m}$) and the 6 cutting speeds (5, 7.5, 10, 20, 30 and 40 m/min)

Table 6: Synthetic quantitative overview of the results: differences between the experimental and the numerical results (average difference for each cutting edge inclination, and maximal, minimal and average differences for all the conditions) for the cutting force, ΔF_c , the feed force, ΔF_f , the passive force, ΔF_p , and the chip thickness ratio, $\Delta \lambda_h$

Difference	ΔF_c (%)	ΔF_f (%)	ΔF_p (%)	$\Delta \lambda_h$ (%)
Average $\lambda_s = 0^\circ$	3	38	—	14
Average $\lambda_s = 6^\circ$	4	40	26	21
Max global	10	60	29	38
Min global	1	10	19	2
Average global	4	39	26	17

onal and free oblique cuts for the titanium alloy Ti6Al4V (the only change is the inclination of the cutting edge). This is a reference to evaluate the performance of the FE 3D model introducing an ANN-based constitutive model developed under the same conditions. A wide range of novel cutting

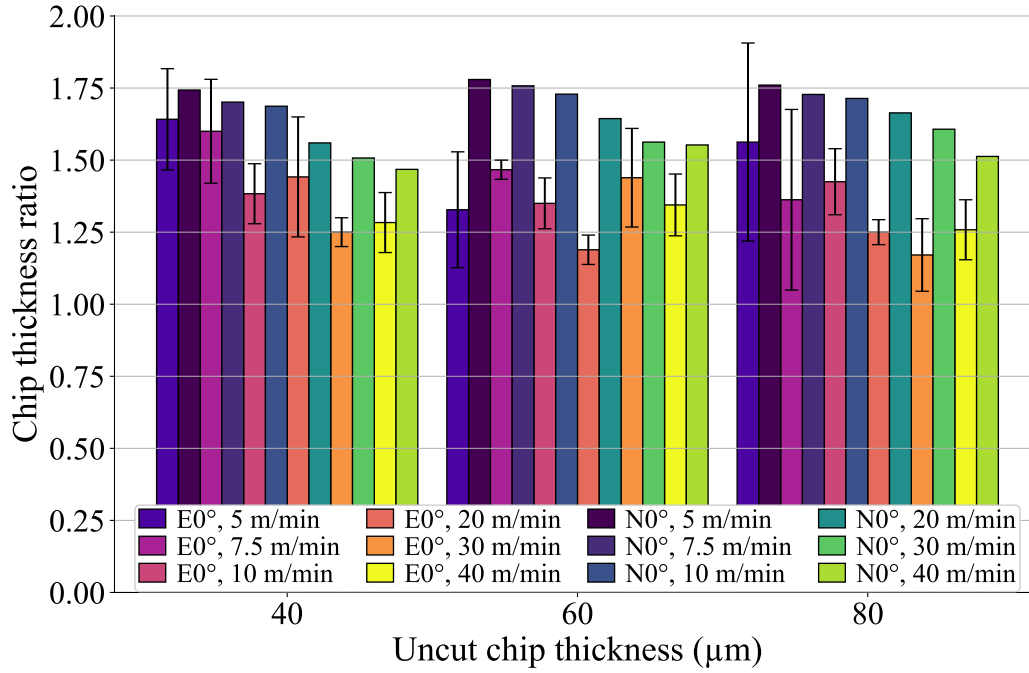


Figure 15: Comparison of experimental (E) and numerical (N) chip thickness ratios at the cutting edge inclination of 6° for the 3 uncut chip thicknesses (40, 60 and 80 μm) and the 6 cutting speeds (5, 7.5, 10, 20, 30 and 40 m/min)

conditions, 36, is considered, including 2 cutting edge inclinations.

- A major novelty of this work is the accurate evaluation of the fundamental variables and their trends in 3D, without the need to adjust the numerical parameters and the model characteristics when the cutting conditions and the inclination angle are changed significantly. The mere fact of changing the inclination angle from free orthogonal cutting to oblique cutting while maintaining the quality of the results has no equivalent in the current literature, especially since no studies (experimental or numerical) on free oblique cutting are available.
- Taking into account the material's flow law by means of a neural network makes it possible to overcome the limitations of conventional flow laws and to reduce the approximations associated with the establishment of an analytical formulation of the flow law as conventionally adopted. The numerical model is then able to better reproduce the real behaviour of the material and

to take into account thermomechanical transformations which are sources of non-linearities, difficult to take into account with an analytical flow law model. Current work, using a Gleeble thermomechanical simulator, on the behaviour of a modified carbon alloy AISI P20 shows the advantages of this approach compared to models in the literature such as Johnson-Cook, Zerilli-Armstrong [16] or Hansel-Spittel [40], insofar as one is then able to better reproduce more complex material behaviour.

- The cutting force is the best modelled quantity with an average difference of 4 % with the experiments. Chip thickness ratio and passive force show a larger deviation from the experiments (17 % and 26 %, respectively), but their trends as the cutting conditions change are accurate. This is in line with the expected results provided by a predictive model. The deviation for feed force is higher (39 %), and opposite trends compared to the experimental reference are observed. The lack of influence of uncut chip thickness on friction in the model seems to be one of the aspects to be included as a priority in future work. The model is found to handle the occurrence of the third force, out of plane, well without significant degradation of the results.
- The predictive capabilities of the model make it suitable for the development of straight-edged tools, for example. This work also demonstrates the ability to model material behaviour with ANN and opens up possibilities in this promising direction.

References

- [1] P. J. Arrazola, T. Özel, D. Umbrello, M. Davies, I. S. Jawahir, Recent advances in modelling of metal machining processes, *CIRP Annals* 62 (2013) 695–718.
- [2] M. Agmell, V. Bushlya, S. V. A. Laakso, A. Ahadi, J.-E. Ståhl, Development of a simulation model to study tool loads in pcBN when machining AISI 316L, *Int J Adv Manuf Technol* 96 (2018) 2853–2865.
- [3] X. Xu, J. Outeiro, J. Zhang, B. Li, W. Zhao, Simulation of material side flow using a 3D coupled Eulerian-Lagrangian approach and a constitutive model considering the stress state, *Procedia CIRP* 102 (2021) 441–446.

- 449 [4] M. Abouridouane, T. Bergs, D. Schraknepper, G. Wirtz, Friction behavior
450 in metal cutting: Modeling and simulation, *Procedia CIRP* 102 (2021) 405–
451 410.
- 452 [5] F. Ducobu, E. Rivière-Lorphèvre, E. Filippi, Experimental contribution to
453 the study of the Ti6Al4V chip formation in orthogonal cutting on a milling
454 machine, *Int J Mater Form* 8 (2015) 455–468.
- 455 [6] A. Sela, G. Ortiz-de-Zarate, D. Soler, G. Germain, P. Aristimuño, P. J. Arra-
456 zola, Measurement of plastic strain and plastic strain rate during orthogonal
457 cutting for Ti-6Al-4V, *International Journal of Mechanical Sciences* 198
458 (2021) 106397.
- 459 [7] M. Afrasiabi, J. Saelzer, S. Berger, I. Iovkov, H. Klippel, M. Röthlin,
460 A. Zabel, D. Biermann, K. Wegener, A Numerical-Experimental Study on
461 Orthogonal Cutting of AISI 1045 Steel and Ti6Al4V Alloy: SPH and FEM
462 Modeling with Newly Identified Friction Coefficients, *Metals* 11 (2021)
463 1683.
- 464 [8] F. Ducobu, E. Rivière-Lorphèvre, E. Filippi, Application of the Coupled
465 Eulerian-Lagrangian (CEL) method to the modeling of orthogonal cutting,
466 *Eur J Mech A Solids* 59 (2016) 58–66.
- 467 [9] F. Ducobu, E. Rivière-Lorphèvre, E. Filippi, Finite element modelling of 3D
468 orthogonal cutting experimental tests with the Coupled Eulerian-Lagrangian
469 (CEL) formulation, *Finite Elements in Analysis and Design* 134 (2017) 27–
470 40.
- 471 [10] D. Ambrosio, A. Tongne, V. Wagner, G. Dessen, O. Cahuc, A new damage
472 evolution criterion for the coupled Eulerian-Lagrangian approach: Applica-
473 tion to three-dimensional numerical simulation of segmented chip formation
474 mechanisms in orthogonal cutting, *Journal of Manufacturing Processes* 73
475 (2022) 149–163.
- 476 [11] A. Vovk, J. Sölter, B. Karpuschewski, Finite element simulations of the
477 material loads and residual stresses in milling utilizing the CEL method,
478 *Procedia CIRP* 87 (2020) 539–544.
- 479 [12] M. Hardt, T. Bergs, Three Dimensional Numerical Modeling of Face Turn-
480 ing Using the Coupled-Eulerian-Lagrangian Formulation, *Procedia CIRP*
481 102 (2021) 162–167.

- 482 [13] S. N. Melkote, W. Grzesik, J. Outeiro, J. Rech, V. Schulze, H. Attia, P.-J.
483 Arrazola, R. M'Saoubi, C. Saldana, Advances in material and friction data
484 for modelling of metal machining, *CIRP Annals* 66 (2017) 731–754.
- 485 [14] G. Johnson, W. Cook, A constitutive model and data for metals subjected
486 to large strains, high strain rates and high temperatures, in: *Proc. 7th Inter-*
487 *national Symposium on Ballistics*, volume 21, The Hague, The Netherlands,
488 pp. 541–547.
- 489 [15] M. Calamaz, D. Coupard, F. Girot, A new material model for 2D numer-
490 ical simulation of serrated chip formation when machining titanium alloy
491 Ti–6Al–4V, *International Journal of Machine Tools and Manufacture* 48
492 (2008) 275–288.
- 493 [16] A. M. Lennon, K. T. Ramesh, On the performance of modified Zerilli-
494 Armstrong constitutive model in simulating the metal-cutting process, *Jour-*
495 *nal of Manufacturing Processes* 28 (2017) 253–265.
- 496 [17] T. Özel, T. Altan, Determination of workpiece flow stress and friction at the
497 chip–tool contact for high-speed cutting, *Int J Mach Tools Manuf* 40 (2000)
498 133–152.
- 499 [18] A. Shrot, M. Bäker, Determination of Johnson–Cook parameters from ma-
500 chining simulations, *Comput Mater Sci* 52 (2012) 298–304.
- 501 [19] F. Klocke, D. Lung, S. Buchkremer, I. S. Jawahir, From Orthogonal Cutting
502 Experiments towards Easy-to-Implement and Accurate Flow Stress Data,
503 *Materials and Manufacturing Processes* 28 (2013) 1222–1227.
- 504 [20] P. Bosetti, C. Maximiliano Giorgio Bort, S. Bruschi, Identification of John-
505 son–Cook and Tresca's Parameters for Numerical Modeling of AISI-304
506 Machining Processes, *J Manuf Sci Eng* 135 (2013).
- 507 [21] B. Denkena, T. Grove, M. A. Dittrich, D. Niederwestberg, M. Lahres, In-
508 verse Determination of Constitutive Equations and Cutting Force Modelling
509 for Complex Tools Using Oxley's Predictive Machining Theory, *Procedia*
510 *CIRP* 31 (2015) 405–410.
- 511 [22] T. Bergs, M. Hardt, D. Schraknepper, Determination of Johnson-Cook ma-
512 terial model parameters for AISI 1045 from orthogonal cutting tests using
513 the Downhill-Simplex algorithm, *Procedia Manuf* 48 (2020) 541–552.

- 514 [23] M. Hardt, D. Schraknepper, T. Bergs, Investigations on the Application of
515 the Downhill-Simplex-Algorithm to the Inverse Determination of Material
516 Model Parameters for FE-Machining Simulations, *Simulation Modelling
517 Practice and Theory* 107 (2021) 102214.
- 518 [24] B. Stampfer, G. González, E. Segebade, M. Gerstenmeyer, V. Schulze, Ma-
519 terial parameter optimization for orthogonal cutting simulations of AISI4140
520 at various tempering conditions, *Procedia CIRP* 102 (2021) 198–203.
- 521 [25] M. Hardt, D. Jayaramaiah, T. Bergs, On the Application of the Particle
522 Swarm Optimization to the Inverse Determination of Material Model Pa-
523 rameters for Cutting Simulations, *Modelling 2* (2021) 129–148.
- 524 [26] N. Kugalur Palanisamy, E. Rivière Lorphèvre, M. Gobert, G. Briffoteaux,
525 D. Tuytens, P.-J. Arrazola, F. Ducobu, Identification of the Parameter Val-
526 ues of the Constitutive and Friction Models in Machining Using EGO Algo-
527 rithm: Application to Ti6Al4V, *Metals* 12 (2022) 976.
- 528 [27] O. Pantalé, P. Tize Mha, A. Tongne, Efficient implementation of non-linear
529 flow law using neural network into the Abaqus Explicit FEM code, *Finite
530 Elements in Analysis and Design* 198 (2022) 103647.
- 531 [28] S. Seo, O. Min, H. Yang, Constitutive equation for Ti–6Al–4V at high tem-
532 peratures measured using the SHPB technique, *Int J Impact Eng* 31 (2005)
533 735–754.
- 534 [29] F. Ducobu, E. Rivière-Lorphèvre, E. Filippi, On the importance of the choice
535 of the parameters of the Johnson-Cook constitutive model and their influence
536 on the results of a Ti6Al4V orthogonal cutting model, *Int J Mech Sci* 122
537 (2017) 143–155.
- 538 [30] GRANTA EduPack 2020, Granta Design Limited, 2020.
- 539 [31] N. Milošević, I. Aleksic, Thermophysical properties of solid phase Ti-6Al-
540 4V alloy over a wide temperature range (2012).
- 541 [32] J. Rech, P. J. Arrazola, C. Claudin, C. Courbon, F. Pusavec, J. Kopac, Char-
542 acterisation of friction and heat partition coefficients at the tool-work mate-
543 rial interface in cutting, *CIRP Annals* 62 (2013) 79–82.

- [33] O. Pantalé, Coefficients of an ANN constitutive flow law of a Ti6-Al-4V material for dynamic applications, Zenodo (2022).
- [34] L. Wang, H. Long, Investigation of material deformation in multi-pass conventional metal spinning, *Materials & Design* 32 (2011) 2891–2899.
- [35] F. Ducobu, E. Rivière-Lorphèvre, E. Filippi, On the introduction of adaptive mass scaling in a finite element model of Ti6Al4V orthogonal cutting, *Simulation Modelling Practice and Theory* 53 (2015) 1–14.
- [36] M. Sima, T. Özel, Modified material constitutive models for serrated chip formation simulations and experimental validation in machining of titanium alloy Ti–6Al–4V, *International Journal of Machine Tools and Manufacture* 50 (2010) 943–960.
- [37] F. Ducobu, E. Rivière-Lorphèvre, E. Filippi, Material constitutive model and chip separation criterion influence on the modeling of Ti6Al4V machining with experimental validation in strictly orthogonal cutting condition, *International Journal of Mechanical Sciences* 107 (2016) 136–149.
- [38] Y. Karpat, Temperature dependent flow softening of titanium alloy Ti6Al4V: An investigation using finite element simulation of machining, *Journal of Materials Processing Technology* 211 (2011) 737–749.
- [39] Y. C. Zhang, T. Mabrouki, D. Nelias, Y. D. Gong, Chip formation in orthogonal cutting considering interface limiting shear stress and damage evolution based on fracture energy approach, *Finite Elements in Analysis and Design* 47 (2011) 850–863.
- [40] K. Chadha, D. Shahriari, M. Jahazi, An approach to develop hansel–spittel constitutive equation during ingot breakdown operation of low alloy steels, in: *Frontiers in materials processing, applications, research and technology*, Springer, 2018, pp. 239–246.

Appendix A. Coefficients of the ANN 3-9-7-1-sig

In this appendix, we present the values obtained after the training phase of an ANN containing 9 neurons in the first hidden layer and 7 neurons in the second hidden layer. Conforming to [27], this one is referred ANN-3-9-7-1-sig. The training of the neural network was performed using a dataset containing 3430 data points defined by :

- 70 equidistant values for $\varepsilon^p \in [0, 3]$, so that $[\varepsilon^p]_{min} = 0$ and $[\varepsilon^p]_{max} = 3$.
- 7 plastic strain rates $\dot{\varepsilon}^p \in [1/s, 10/s, 50/s, 500/s, 5000/s, 50\,000/s, 500\,000/s]$, so that $[\ln(\dot{\varepsilon}^p)]_{min} = 0$ and $[\ln(\dot{\varepsilon}^p)]_{max} = 13.12236$.
- 7 temperatures $T \in [293\text{ K}, 400\text{ K}, 500\text{ K}, 700\text{ K}, 900\text{ K}, 1200\text{ K}, 1500\text{ K}]$, so that $[T]_{min} = 293\text{ K}$ and $[T]_{max} = 1500\text{ K}$.

Stresses in the training dataset ranges from $[\sigma^y]_{min} = 171.4\text{ MPa}$ to $[\sigma^y]_{max} = 2606.1\text{ MPa}$. The results of the training process are given here after for the ANN quantities \mathbf{W}_1 , \mathbf{W}_2 , \vec{w} , \vec{b}_1 , \vec{b}_2 and b . The weight matrix for the first hidden layer \mathbf{W}_1 is a 9×3 matrix:

$$\mathbf{W}_1 = \begin{bmatrix} -0.87229 & -0.47675 & -1.50771 \\ -0.95762 & -0.25619 & 1.65222 \\ -10.61660 & 0.22003 & -0.11539 \\ 3.67883 & 0.37146 & -1.51069 \\ -63.39468 & 0.15466 & -0.95431 \\ 0.54807 & 0.25959 & -5.44355 \\ -1.33883 & 0.36089 & -1.66735 \\ -0.68125 & 1.02121 & 0.34242 \\ 0.08740 & 0.18764 & -41.32542 \end{bmatrix}$$

The weight matrix for the second hidden layer \mathbf{W}_2 is a 7×9 matrix:

$$\mathbf{W}_2^T = \begin{bmatrix} 1.66285 & -0.59645 & -3.17333 & 0.20706 & 1.18760 & 2.01250 & -0.82147 \\ -0.26237 & -2.50330 & -1.45941 & -1.59833 & 4.05169 & -1.21146 & 1.05610 \\ -0.12958 & 0.67119 & -5.85989 & -2.55061 & 4.85245 & 4.31876 & 3.24070 \\ -2.12890 & 0.68296 & 0.71183 & 0.81706 & -0.09405 & 0.34919 & -1.41223 \\ 2.33631 & -0.08089 & 14.65789 & 0.12531 & 23.66363 & 2.55872 & 2.15338 \\ 0.11567 & 1.77629 & -1.80448 & 0.77825 & -1.58254 & 1.90442 & 1.23152 \\ 1.49265 & 0.41821 & -3.53803 & -0.48705 & -0.23671 & 0.75887 & -0.37441 \\ 0.95990 & 0.69041 & 0.43870 & 0.28393 & -1.40101 & -0.64569 & -0.38964 \\ 5.89937 & -0.13015 & 2.99264 & 1.78534 & -3.90189 & 1.17494 & -3.78854 \end{bmatrix}$$

The weight vector for the output layer \vec{w} is a 7 components vector:

$$\vec{w} = \begin{bmatrix} 0.34701 \\ 1.42079 \\ -0.96564 \\ 0.62467 \\ -0.56322 \\ 0.40960 \\ -0.42810 \end{bmatrix}$$

The biases of the first hidden layer \vec{b}_1 is a 9 components vector:

$$\vec{b}_1 = \begin{bmatrix} 2.57141 \\ 0.22673 \\ -1.16985 \\ -0.11246 \\ -0.82210 \\ -2.13264 \\ 0.78794 \\ 1.20434 \\ -3.48681 \end{bmatrix}$$

The biases of the second hidden layer \vec{b}_2 is a 7 components vector:

$$\vec{b}_2 = \begin{bmatrix} -0.36566 \\ -1.14445 \\ -0.79065 \\ -0.50670 \\ 1.30136 \\ 0.04521 \\ -0.29995 \end{bmatrix}$$

The bias of the output layer b is a scalar:

$$b = 0.04213$$

587 The corresponding coefficients for the other networks identified during this
588 work (ANN-3-11-7-1-sig, ANN-3-13-7-1-sig, ANN-3-15-7-1-sig and ANN-3-17-
589 7-1-sig) can be found in [33].